Dual Li^+ transport enabled by BN-assisted solid-polymer-electrolyte for high-performance lithium batteries

Yuchen Wang [a,b], Haifeng Tu [a,b], Ao Sun [a], Lu Wang [a], Fengyi Zhu [a], Pan Xue [c], Jian Wang [d], Fangmin Ye [e,*], Meinan Liu [a,f,g,*]

[a] Key Laboratory of Multifunctional Nanomaterials and Smart Systems, Suzhou Institute of Nano-Tech and Nano-Bionics, Chinese Academy of Sciences, Suzhou, Jiangsu 215123, China
[b] Nano Science and Technology Institute, University of Science and Technology of China, Hefei, Anhui 230026, China
[c] School of Chemistry and Chemical Engineering, Yangzhou University, Yangzhou 225002, China
[d] Helmholtz Institute Ulm, (HIU), Ulm 89081, Germany
[e] Key Laboratory of Optical Field Manipulation of Zhejiang Province, Department of Physics, Zhejiang Sci-Tech University, Hangzhou 310018, China
[f] Division of Nanomaterials and Jiangxi Key Lab of Carbonene Materials, Jiangxi Insitute of Nanotechnology, Nanchang 330200, China
[g] Guangdong Institute of Semiconductor Micro-nano Manufacturing Technology, Foshan 528225, China

Keywords:
Li^+ transportation kinetics
BN-assisted solid-polymer electrolyte
Solvation structure
Lithium metal battery

A B S T R A C T

Solid-state lithium batteries are expected to revolutionize the future wearable electronics due to their enhanced safety and high energy density; however, the sluggish Li^+ kinetics of solid-state electrolyte seriously hampered their practical applications. Herein, we design a solid-polymer-electrolyte (SPE) with the assistance of BN, which exhibits impressive electrochemical properties, i.e., a high ionic conductivity of 0.37 mS cm^{-1} at 25 °C, a superior Li^+ transference number of 0.63, and wide voltage window of 4.8 V. Density functional theory calculations and Raman spectra results reveal that BN not only changes the interaction between Li^+ and -CF groups, which enables Li^+ to hop easily along polymer segments, but also modifies the Li^+ solvation environment from polymer units to aggregated ion pairs, which further accelerates the diffusion rate of Li^+. Benefited from these merits, BN-assisted SPE presents superior performance at room temperature, i.e., Li/Li symmetric batteries maintain uniform polarization for more than 600 h at a current density of 0.2 mA cm^{-2}; $LiFePO_4$/Li battery delivers an excellent long cycle stability with a high Coulombic efficiency (CE) of 99.7 % at 0.5C after 200 cycles; the high-voltage $LiNi_{0.5}Co_{0.2}Mn_{0.3}O_2$/Li system also achieves a superior CE of 99.7 % and, what's more, this system also delivers a high-capacity retention of 90 % over 100 cycles, indicating the outstanding antioxidation capability of this BN-assisted SPE. In addition, a bipolar $LiFePO_4$/Li pouch cell with a high-voltage output of 6.41 V was achieved and it demonstrates impressive safety during the abuse cutting, well demonstrating its great potential in future applications.

1. Introduction

With the development of wearable and portable electric devices, rechargeable and safe batteries with high energy density are highly demanded. Unfortunately, current lithium-ion batteries (LIBs), such as $LiCoO_2$/Graphite and $LiFePO_4$/Graphite systems, have almost reaching their capacity ceiling [1–4], therefore new battery systems with high theoretical capacity are urgent to be developed. Lithium metal batteries (LMBs) are strongly considered as the next generation of high energy density batteries because the Li anode possesses high theoretical capacity (3860 mAh g^{-1}) and the lowest negative electrochemical potential (-3.040 V vs the standard hydrogen electrode) [5–9]. It should be noted that the uncontrolled parasitic side reactions between Li and liquid electrolyte not only irreversibly consumes Li anode and thus, lead to a short cycle life, but also induces the formation of lithium dendrites, bringing serious safety problems such as flammability and explosion [10–14]. In order to address these issues, solid-state electrolyte (SSE) is regarded as an ideal substitute for liquid electrolytes, since the side reactions between Li anode and electrolyte can be avoided once a robust solid electrolyte interface (SEI) is formed [15–17]; therefore, the safety

* Corresponding authors at: Key Laboratory of Multifunctional Nanomaterials and Smart Systems, Suzhou Institute of Nano-Tech and Nano-Bionics, Chinese Academy of Sciences, Suzhou, Jiangsu 215123, China (M. Liu).
E-mail addresses: fmye2013@sinano.ac.cn (F. Ye), mnliu2013@sinano.ac.cn (M. Liu).

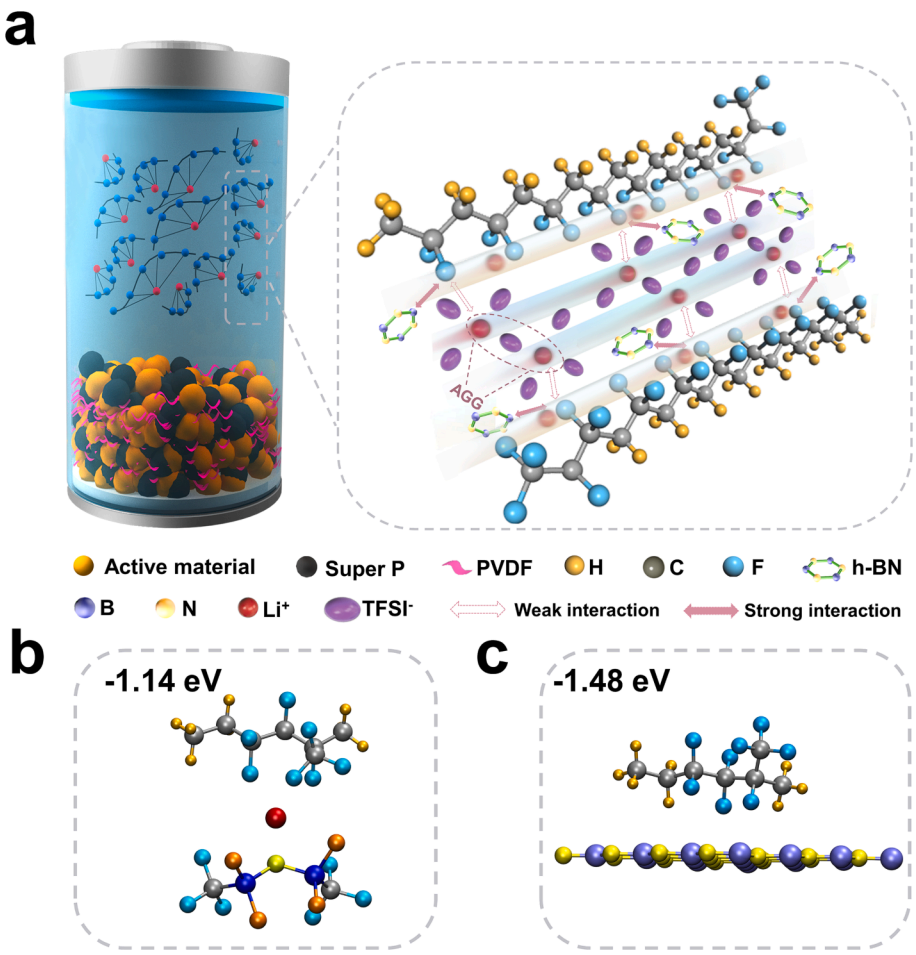

Fig. 1. (a) Schematic illustrations of the Li^+ transport pathway of the as-designed PHLBH electrolyte. (b) The adsorption energy of dissociated Li^+ ions on PVDF-HFP. (c) The adsorption energy of h-BN on PVDF-HFP.

of LMBs with SSE will be dramatically improved.

Among all the SSEs, solid-polymer-electrolytes (SPEs) have attracted a wide range of attention by the low cost, high flexibility, large-scale manufacturing process compatibility, as well as conformal interface with electrodes [18–20]. Recently, the development of SPEs moves towards self-healing, higher energy density (lower N/P ratio), and easier scaling-up producing technique [21–24]. For example, UV-cured composite polymer electrolyte benefited from quadruple hydrogen bond shows strong self-healing property, which dramatically enhances the safety of LMB in practical application [22]. Dynamic poly(urea-urethane) gel electrolyte was also reported that it not only presents superior safety contributed by its self-healing ability, but also delivers impressive ionic conductivity, even higher than that of commercial liquid electrolyte [23]. Moreover, apart from LMB systems, SPEs also present great potential in other metal batteries. Bella et al reported photocured gel polymer electrolyte with a high ionic conductivity of 17 mS cm^{-1} for the application in potassium batteries to achieve unprecedented 600 cycles with a capacity retention of 58 % [25]. Moreover, biobased polymer electrolytes were developed based on cardanol-derived epoxy resins, which present excellent electrochemical stability toward potassium metal in 0.2 ~ 5 V [26]. All these research works well demonstrate the great potential of SPEs in high-energy metal battery systems.

Although SPEs exhibit lots of merits, their ionic conductivities are quite disappointing (<10^{-6} S cm^{-1}) at 25 °C. Moreover, their Li^+ transference numbers are also inferior (~0.3) [27,28], which make SPEs unqualified for practical applications. Besides, the ionic transport mechanism of SPE is based on the hopping of Li^+ between solvation sites composed by polymer functional groups, such as typical ether oxygens (EO) groups in poly(ethylene oxide) (PEO), and Li^+ hopping rate depends on the segmental mobility of the polymer chains [29]. To enhance the hopping rate, researchers introduce various fillers into SPEs [19] or design complex polymer segments [6,30] for creating more amorphous regions in polymer chain, thus enabling Li^+ hopping easily. Indeed, the ionic conductivity of SPEs can be enhanced based on these treatments, but they are still far from the value required for working at 25 °C [31]. How to further improve the Li^+ hopping rate in polymer chains is still a big challenge.

Recently, aggregated ion pairs (AGG, an anion coordinating with two or more Li^+) with their unique Li^+ transport mechanism attract much attention. Normally, the Li^+ solvation structure is composed by solvent molecules (solvent-separated ion pairs, SSIP), while it can turn into combination of solvent molecules and anions, such as AGG with the increase of lithium salt concentration [32,33]. Different from the vehicle diffusion mechanism of Li^+ with SSIP, AGG solvation structure refers to Grotthuss mechanism, which enables Li^+ transporting much faster [34]. Therefore, constructing AGG solvation structure seems to be an efficient way to enhance Li^+ mobility in SPEs. High-concentrated lithium salt method has been proved to be the simplest way to achieve AGG structure. For example, Liu et al. successfully developed a SPE with AGG structure based on high-concentrated lithium bis(trifluoromethanesulphonyl)imide (LiTFSI) and poly(vinylidene fluoride-*co*-hexafluoropropylene) (PVDF-HFP) with a weight ratio of LiTFSI/PVDF-HFP around 1.1, which contributes to a high ionic conductivity of 0.124 mS cm^{-1} at 25 °C [35]. Unfortunately, further increasing concentration of lithium salt will decay the performance of SPE since the

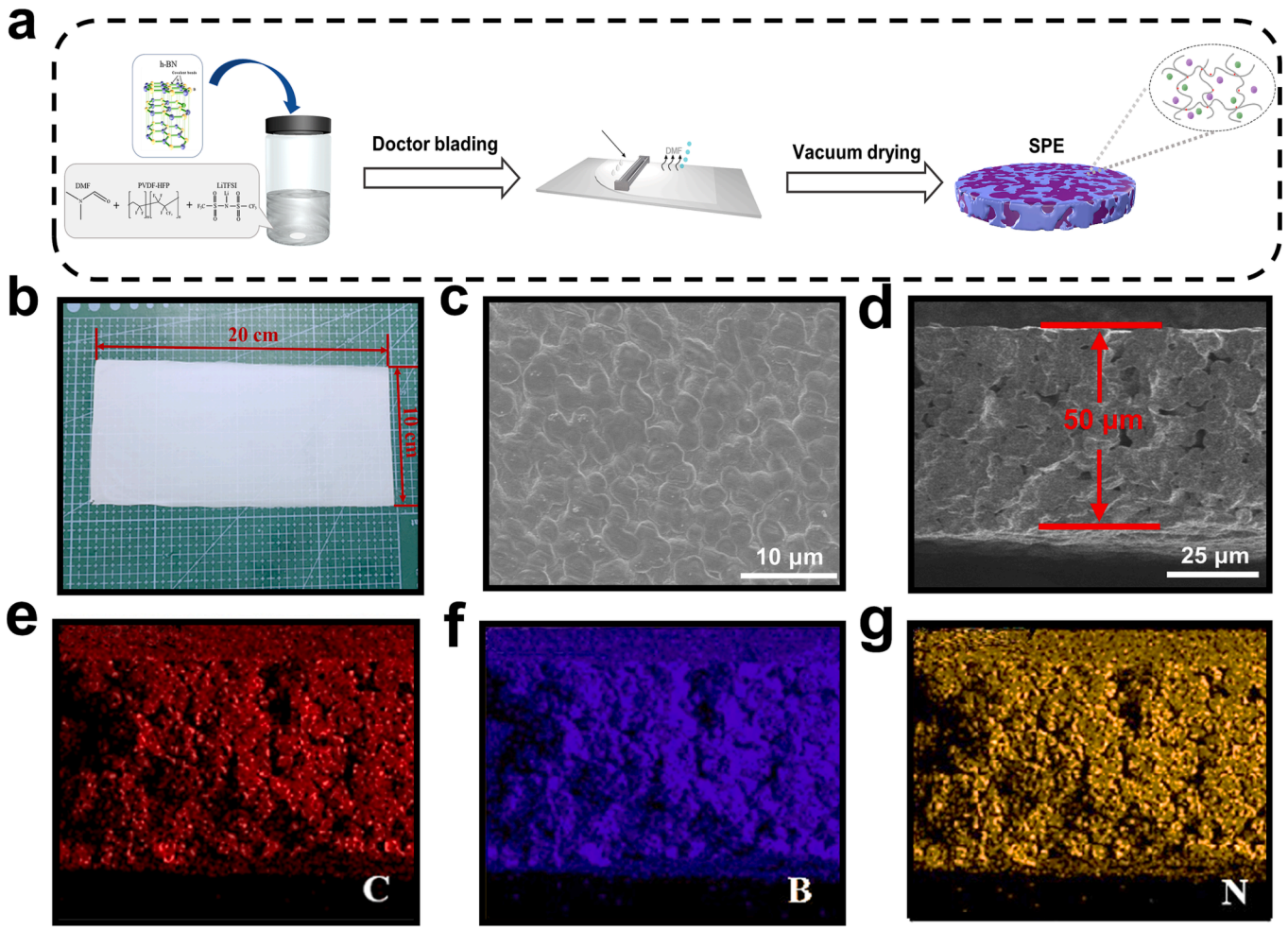

Fig. 2. (a) Schematic illustration of the synthesis of PHL and PHLBN electrolytes. (b) Digital photograph of a large-scale $PHL_{1.25}BN_5$ membrane. (c) SEM image of $PHL_{1.25}BN_5$ electrolyte surface. (d) SEM image of $PHL_{1.25}BN_5$ membrane in side-view. (e–g) EDS elemental mappings of C, B and N in $PHL_{1.25}BN_5$ membrane.

high concentration of lithium salt not only suppresses segmental motion of polymer chain due to the ion-polymer "crosslinking", but also deteriorates the dissociation of lithium salt. To avoid the bad effect of high-concentrated lithium salts, a delicate strategy on manipulating the intermolecular interactions was designed in our previous work through introducing $Li_{1.3}Al_{0.3}Ti_{1.7}(PO_4)_3$ (LATP) to tune the solvation environment of Li^+ for constructing AGG structure, and finally dramatically enhances the ionic conductivity to 0.73 mS cm ^{1} [36].

Based on the above analysis, it can be concluded that an ideal SPE should possess two types of Li^+ transportation channels: one is along the polymer chain with fast Li^+ hopping rate and the other is the internal cluster channel created by AGG solvation structure. Is there any possibility to design a simple SPE system with these two types of transport path for fast Li^+ diffusion kinetics? In this work, SPE with dual ionic transportation channels has been designed through hexagonal boron nitride (h-BN)-assisted PVDF-HFP and LiTFSI (LiTFSI/PVDF-HFP) system. As shown in Fig. 1, the interaction of PVDF-HFP/BN is stronger than that of PVDF-HFP/LiTFSI, which may weaken the hopping energy of Li^+ along PVDF-HFP chain, and thus enhances Li^+ mobility. Moreover, these BN additives also change Li^+ solvation structure from PVDF-HFP unit to PVDF-HFP/anions, as evidenced by Raman results. The abundant AGG creates another faster Li^+ diffusion pathway, which further enhances Li^+ transport kinetics in SPE. Benefited from these two types of Li^+ transport channels, the as-fabricated PVDF-HFP/LiTFSI/BN (PHLBN) SPE presents impressive ionic conductivity (3.7×10^{4} S cm ^{1}), high t_{Li+} (0.63) and wide electrochemical window (~4.8 V) at 25 ℃. Applying this PHLBN to a LMB system, the cycle life of Li|PHLBN|Li cell can be extended to as long as 800 h at 0.1 mA cm ^{2} and 600 h at 0.2 mA cm ^{2}. The Li|PHLBN|$LiFePO_4$ (LFP) cell delivers a Coulombic efficiency of 99.7 % after 200 cycles under 25 °C. Furthermore, pairing with high-voltage NCM523 ($LiNi_{0.5}Co_{0.2}Mn_{0.3}O_2$) as a cathode, NCM523/Li cells can still achieve a superior capacity retention of 90 % (127 mAh g ^{1}) after 100 cycles at 0.5C under 25 ℃. Thanks to the excellent stability and easy-processing, PHLBN can also be facilely assembled into bipolar LFP/Li pouch cell, which not only supports high-voltage output (6.41 V), but also exhibits excellent safety under abuse tests (folding and cutting), demonstrating the great potential in future practical applications.

2. Results and discussion

H-BN with boron and nitride atoms arranged in a two-dimensional honeycomb lattice structure seems to be a magic material. Lately, it has been found that these N atoms with strong electron-withdrawing effect working together with the B atoms with Lewis acidic properties effectively limit the movement of anions in electrolyte system [37,38], which may promote the dissociation of lithium salt in SPE. To examine whether BN shows great influence in LiTFSI/PVDF-HFP system, density functional theory (DFT) calculation was employed to study the interaction among BN, LiTFSI and PVDF-HFP. As shown in Fig. 1b, the adsorption energy of dissociated Li^+ ions and h-BN on PVDF-HFP is 1.14 eV and 1.48 eV, respectively. This result well suggests a stronger interaction between PVDF-HFP and h-BN compared to PVDF-HFP and Li^+. While the weak interaction in PVDF-HFP/Li^+ may benefit for these

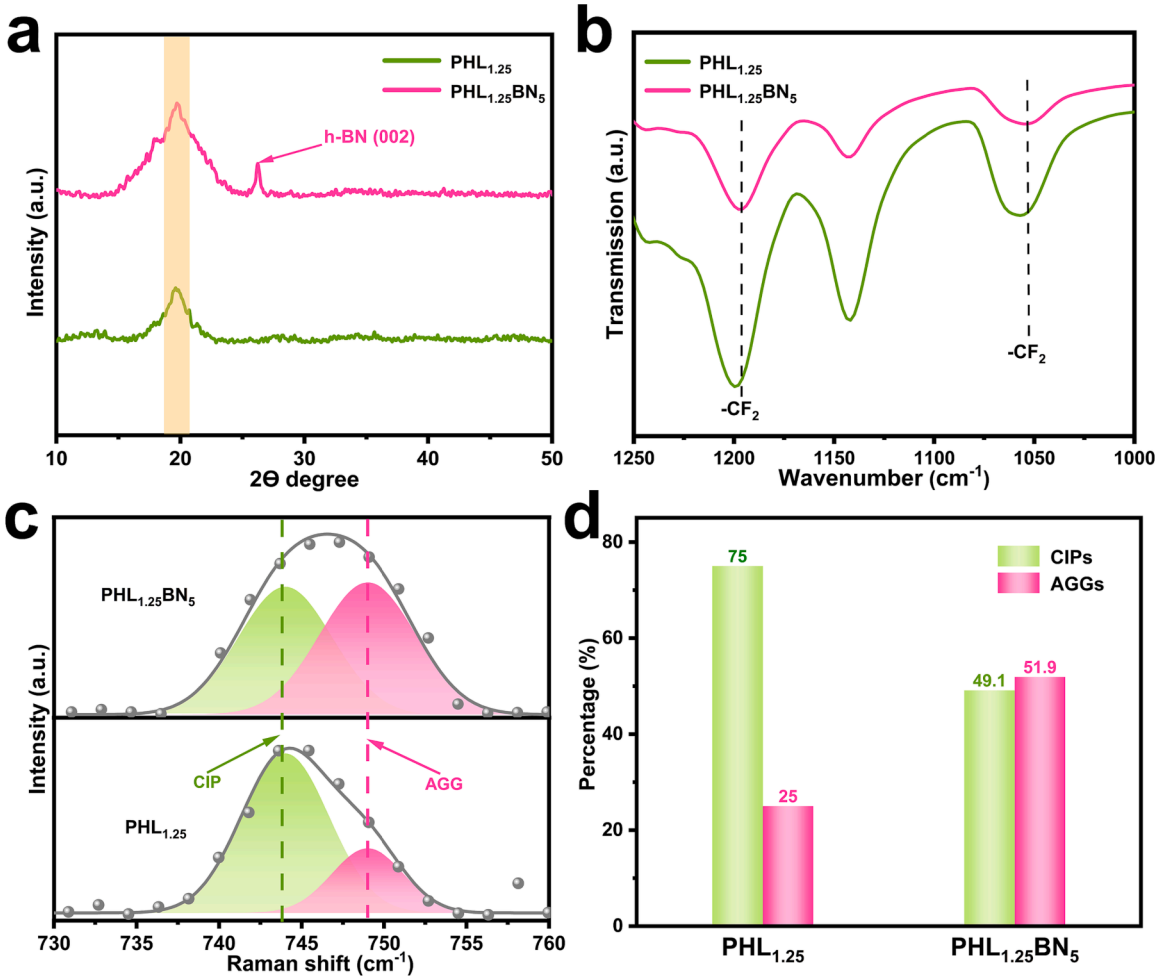

Fig. 3. (a) XRD patterns of $PHL_{1.25}$ and $PHL_{1.25}BN_5$ electrolytes. (b) FTIR spectra of $PHL_{1.25}$ and $PHL_{1.25}BN_5$ electrolytes. (c) Raman spectra and fitting curves of $PHL_{1.25}$ and $PHL_{1.25}BN_5$ electrolytes in the range of 730–760 cm^{-1} (S—N stretching, C—S stretching, and CF_3 bending vibration mode of $TFSI^-$). Solid lines denote experimental spectra and shadow sections represent the fitting peak (CIP: contact ion pair, AGG: aggregated ion pair). (d) The quantitative analysis of CIPs and AGGs of $PHL_{1.25}$ and $PHL_{1.25}BN_5$ electrolytes.

dissociated Li^+ ions hopping along polymer segments.

Based on the above calculation suggestions, BN-assisted PVDF-HFP/LiTFSI SPE was designed and developed. PVDF-HFP was selected as a polymer due to its high dielectric constant and ionic conductivity [39]. The fabrication process of PHLBN is illustrated in Fig. 2a. Firstly, PVDF-HFP and LiTFSI were dissolved in N,*N*-dimethylformamide (DMF) to form clear solution, then BN was added to form white slurry (Fig. S1). Finally, PHLBN membrane can be obtained through casting the slurry on a glass substrate by doctor blade method. To investigate the working mechanism of BN, a control sample PVDF-HFP/LiTFSI (PHL) membrane without BN was also prepared. As discussed above, salt concentration has a great influence on the ionic conductivity of polymer electrolytes. In Fig. S2, it can be found that ionic conductivity of PHL-0.5 (0.0047 mS cm ^{1}), PHL-0.75 (0.025 mS cm ^{1}), PHL-1 (0.054 mS cm ^{1}), PHL-1.25 (0.097 mS cm ^{1}) and PHL-1.5 (0.108 mS cm ^{1}) increases with salt mass ratio. Unfortunately, a higher salt concentration may deteriorate the mechanical property of SPE. A shown in Fig. S3, it can be clearly observed that pure PHL-1.5 membrane is broken, well indicating its poor mechanical property. Therefore, PHL-1.25 was selected as the optimized composition considering the trade-off between ionic conductivity and mechanical property. To further enhance the ionic conductivity of PHL, BN was introduced to form PHLBN. Differential scanning calorimetry tests present that the glass transportation temperatures (T_g) of PHLBN (with 5 wt% BN) and PHL are 90 and 136 °C, respectively. The lower T_g in PHLBN well indicates that the introduction of BN enhances the amorphous regions in PVDF-HFP, which will efficiently promote the motion of polymer chain segments (Fig. S4). Indeed, the ionic conductivity of PHLBN increases with the BN mass ratio, but it drops later (Fig. S5). The highest ionic conductivity of 0.37 mS cm ^{1} can be achieved by adding 5 % BN, which is 3.8 times higher than that PHL-1.25 (0.097 mS cm ^{1}) and almost 3 times higher than that of reported high-concentrated salt system (0.124 mS cm ^{1}) [35]. The decrease of ionic conductivity with 6 % BN (0.197 mS cm ^{1}) suggests that high BN concentration affects these PVDF-HFP solvation sites. Based on the above results, $PHL_{1.25}BN_5$ (PHL-1.25 with 5 % BN) as the optimized SPE was investigated in the following study and $PHL_{1.25}$ was also studied for comparison.

Benefiting from the simple fabrication process, $PHL_{1.25}BN_5$ and $PHL_{1.25}$ could be easily scaled up [40]. As shown in Fig. 2b, $PHL_{1.25}BN_5$ membrane with a size of 20 cm in length and 10 cm in width can be easily achieved, making the designed electrolytes extremely suitable for the practical application. Moreover, this large size membrane indicates the excellent reproducibility of SPE. The detailed structure of this $PHL_{1.25}BN_5$ membrane was studied by scanning electron microscopy (SEM). It can be found that the top surface of $PHL_{1.25}BN_5$ is quite dense (Fig. 2c) comparing to $PHL_{1.25}$ (Fig. S6). The defect-free $PHL_{1.25}BN_5$ may provide efficient Li^+ pathway. The side view in Fig. 2d suggests that the thickness of $PHL_{1.25}BN_5$ is around 50 μm, which enables the membrane to be quite flexible as shown in Fig. S7. The mechanical property test shows that the stress and strain of $PHL_{1.25}BN_5$ is around 2.25 MPa and

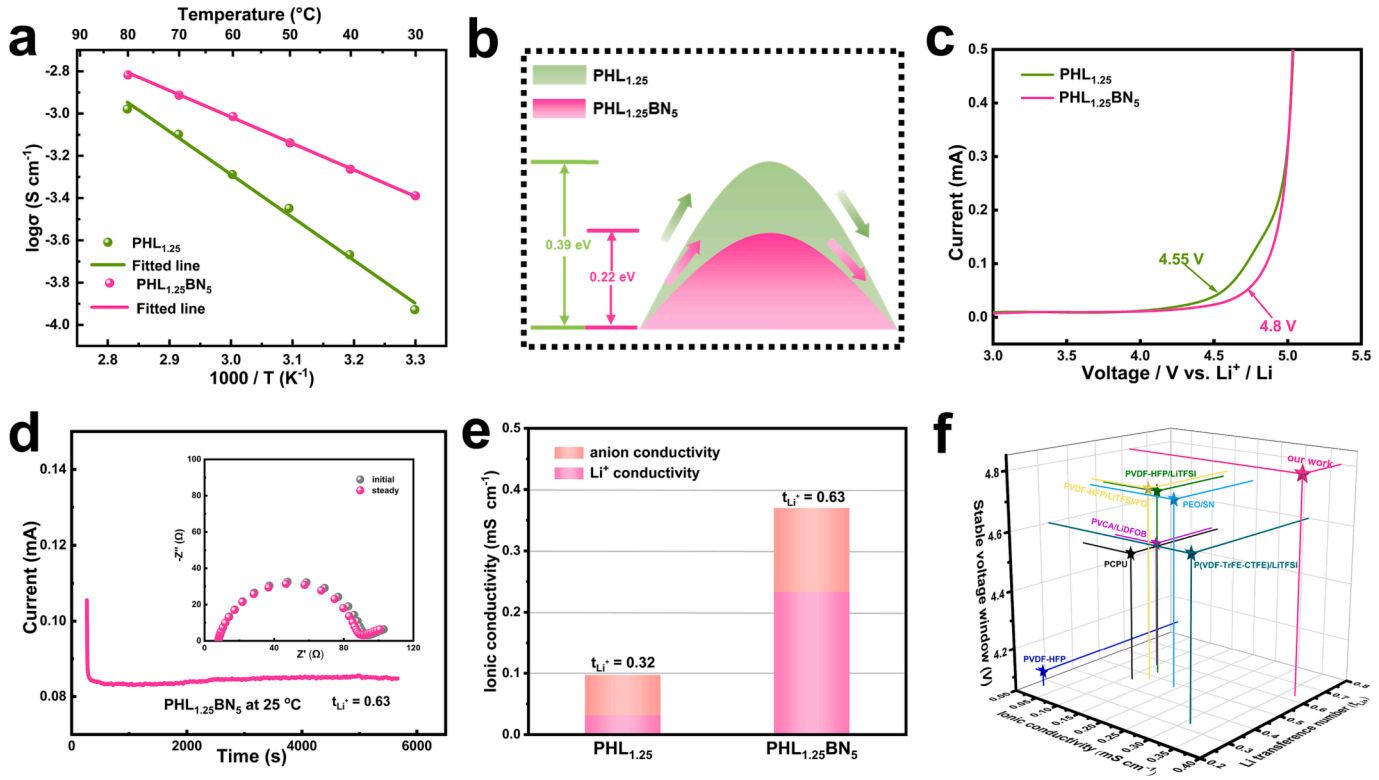

Fig. 4. (a) Arrhenius plots of the ionic conductivities of $PHL_{1.25}$ and $PHL_{1.25}BN_5$ electrolytes in temperature range of 30–80 °C. (b) The activation energy (E_a) of $PHL_{1.25}$ and $PHL_{1.25}BN_5$ electrolytes. (c) LSV curves of $PHL_{1.25}$ and $PHL_{1.25}BN_5$ electrolytes. (d) Li^+ transference number measurement of $PHL_{1.25}BN_5$ electrolyte. (e) Ionic conductivity and Li^+ transfer number of two different electrolytes systems. (f) Comparing the electrochemical performance of the recently reported work with our work. More information can be found in Table S1.

110.5 %, respectively, which are superior to those of $PHL_{1.25}$ (1.5 MPa, 48 %), indicating these BN additives dramatically improve the mechanical property of membrane (Fig. S8). The distribution of BN in PHL was further studied by energy dispersive spectroscopy (EDS) mapping. As shown in Fig. 2e–g, it can be found that BN is distributed homogeneously inside the PVDF-HFP matrix, according to elements C, B and N.

X-ray diffraction (XRD) analysis confirms the successful addition of BN in PVDF-HFP/LiTFSI system (Fig. 3a). No diffraction peaks from LiTFSI are detected in both $PHL_{1.25}$ and $PHL_{1.25}BN_5$ membranes, indicating the dissociation of LiTFSI in PVDF-HFP matrix. In addition, the remarkably broad peaks observed at 18° ~ 20° could be attributed to the interaction between the molecular chains of PVDF-HFP and BN, which also increases the intensity of the peaks at 19.8° [41]. What more, to further explore the molecular interaction in $PHL_{1.25}BN_5$ electrolyte, Fourier transform infrared spectrometer (FTIR), solid-state nuclear magnetic resonance (NMR) spectra of ^6Li and Raman spectra were conducted. As shown in Figs. 3b and S9, the vibrations at 1096 and 1053 cm ^{1} correspond to symmetrical stretching of $-CF_2$, which take a red shift after introducing BN into the PHL electrolyte, confirming the interaction between BN and PVDF-HFP. ^6Li NMR was used here to investigate the lithium environment. As shown in Fig. S10, the peak at 0.41 ppm corresponds to the resonance between Li^+ and PVDF-HFP segments. Meanwhile, the ^6Li sign shows an obvious upfield shift from 0.41 ppm to 0.26 ppm after introducing h-BN, indicating that the interaction between PVDF-HFP and Li^+ is weakened [42,43]. To further study Li^+ coordination environment in SPE, Raman spectra was used here to characterize TFSI . It has been well known that TFSI consists of three different dissociation states: free TFSI at 740 cm ^{1}, contact ion pairs (CIPs) at 744 cm ^{1} (TFSI interacting with a single Li^+) and aggregated ion pairs (AGGs) at 749 cm ^{1} (TFSI interacting with two or more Li^+) [44,45]. The dissociation states of TFSI in both $PHL_{1.25}BN_5$ and $PHL_{1.25}$ samples are dominated by CIP and AGG, as shown in Figs. 3c and S11. The quantitative analysis demonstrates that $PHL_{1.25}$ is composed by 75 % CIP and 25 % AGG, while $PHL_{1.25}BN_5$ consists of 49.1 % CIP and 51.9 % AGG (Fig. 3d). The significant enhancement on AGG in $PHL_{1.25}BN_5$ can be attributed to BN, which effectively tunes the ionic solvation environment. These abundant AGG in $PHL_{1.25}BN_5$ may accelerate Li^+ transportation kinetics, and thus delivers a superior electrochemical property.

To study the electrochemical performances of $PHL_{1.25}BN_5$, a variety of tests were performed. The most vital property parameter for SPE is the ionic conductivity. As shown in Fig. 4a, it can be found that $PHL_{1.25}BN_5$ delivers higher ionic conductivity in all temperature range than $PHL_{1.25}$ (25 ~ 80 °C). Specifically, $PHL_{1.25}BN_5$ shows an ionic conductivity of 0.37 mS cm ^{1} at 25 °C, which is 3.8 times higher than that of $PHL_{1.25}$ (0.097 mS cm ^{1}). Correspondingly, the activation energy (E_a) of $PHL_{1.25}BN_5$ calculated by Arrhenius equation is 0.22 eV, which is lower than that of $PHL_{1.25}$ (0.39 eV), as shown in Figs. 4b and S13, implying that fast ionic transportation channels induced by BN/PVDF-HFP and BN/LiTFSI interfaces greatly decrease the E_a of Li^+ migration [46–48]. The linear sweep voltammetry (LSV) measurements demonstrate that $PHL_{1.25}BN_5$ can work till to 4.8 V, higher than $PHL_{1.25}$ (4.55 V), as presented in Fig. 3c. This high-voltage window is also contributed to BN, which suppresses the decomposition of PVDF-HFP under high voltage. Moreover, BN also enhances the thermal property of $PHL_{1.25}BN_5$, as evidenced by the heating test and thermal gravimetric analysis (TGA). As shown in Fig. S14, Celgard membrane and $PHL_{1.25}$ electrolyte start to melt at 140 °C; but $PHL_{1.25}BN_5$ electrolyte is quite stable under the same temperature. Impressively, it can endure up to 200 °C. The excellent thermal stability well matches with the TGA results shown in Fig. S15, revealing the important role of BN in safety enhancement.

Another important electrochemical parameter for SPE is Li^+ transference number (t_{Li}^+). Normally, the t_{Li+} of SPEs is low (<0.3), due to the Lewis base centers of the polymer coupling with Li^+, causing its sluggish

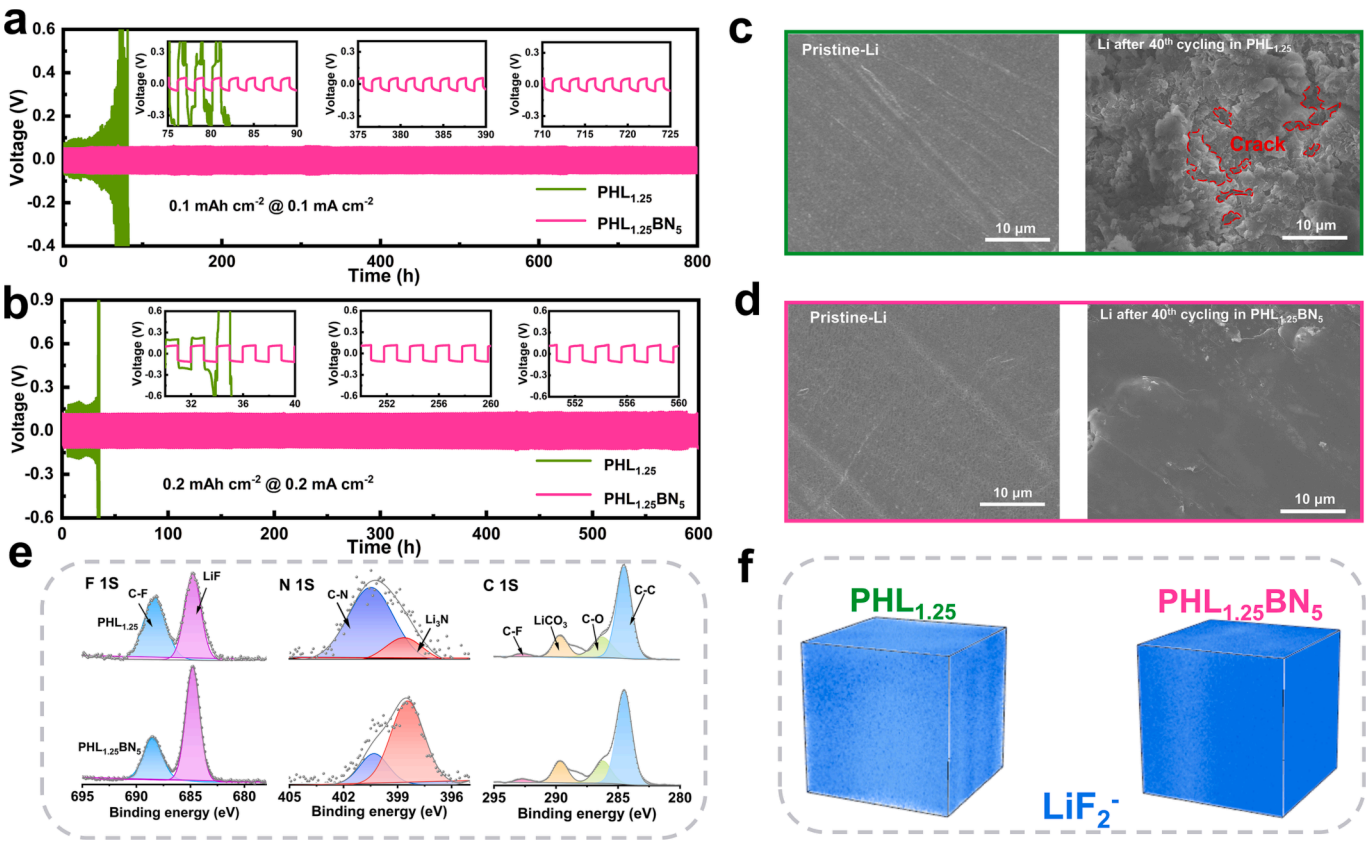

Fig. 5. (a, b) Long-term voltage profiles of Li/Li batteries at a current density of 0.1 mA cm^{-2} and 0.2 mA cm^{-2} with $PHL_{1.25}$ and $PHL_{1.25}BN_5$ electrolytes under 25 °C. (c) SEM images of pristine Li anode surface and after 40th cycling in Li|$PHL_{1.25}$|Li system at 0.1 mA cm^{-2}. (d) SEM images of pristine Li anode surface and after 40th cycling in Li|$PHL_{1.25}BN_5$|Li system at 0.1 mA cm^{-2}. (e) XPS spectra of F 1 s, N 1 s and C 1 s of the surface of cycled Li metal after 40 cycles at 0.1 mA cm^{-2}. (f) The 3D reconstruction distribution map of the LiF_2^- of cycled Li surface formed in $PHL_{1.25}$ and $PHL_{1.25}BN_5$ electrolyte systems.

mobility [49]. In this work, the t_{Li+} of $PHL_{1.25}BN_5$ is calculated to be 0.63, which is almost twice higher than that of $PHL_{1.25}$ (0.32), indicating the excellent mobility of Li^+ in $PHL_{1.25}BN_5$ (Fig. S16). Fig. 4f and Table S1 present the comparison of our $PHL_{1.25}BN_5$ with previous reported SPEs from three aspects, i.e., ionic conductivity, t_{Li+} and stable voltage window. Surprisingly, this simple $PHL_{1.25}BN_5$ shows the best electrochemical properties.

Considering the above merits of $PHL_{1.25}BN_5$, it is also expected to behave efficiently in batteries. Symmetric Li/Li cells were used to evaluate the interfacial stability of electrolyte against Li anode and suppressing capability on lithium dendrites. As shown in Fig. S17, the electrochemical impedance spectroscopy (EIS) of these two systems reveals that the interface resistance of $PHL_{1.25}BN_5$ system is 93 Ω, almost half of $PHL_{1.25}$ system (195 Ω). The lower interface resistance demonstrates the efficient Li^+ transportation kinetics in $PHL_{1.25}BN_5$, which is consistent with the above electrochemical properties. In Fig. S18, it can be found that the overpotential increases with the current density increasing from 0.025 to 0.1 mA cm^{-1} in both cells, but the overpotential of Li|$PHL_{1.25}$|Li is much higher than that of Li|$PHL_{1.25}BN_5$|Li at all current densities under 25 °C, suggesting that $PHL_{1.25}BN_5$ is compatible with Li anode. Indeed, Li/Li cell with $PHL_{1.25}$ appears short-circuit phenomenon at 309 h at 0.05 mA cm^{-1}, while Li|$PHL_{1.25}BN_5$|Li can maintain stable till to 1100 h (Fig. S19). Further increasing the current density to 0.1 mA cm^{-1}, Li|$PHL_{1.25}$|Li battery shows very jerky voltage curve and its polarization voltage increases sharply after 80 h, suggesting the failure of cell caused by lithium dendrites. In contrast, the overpotential of Li|$PHL_{1.25}BN_5$|Li system is around 60 mV and it can remain stable up to 800 h without obvious fluctuation. Even under the current density of 0.2 mA cm^{-2}, this $PHL_{1.25}BN_5$ system could also cycle up to 600 h; while the control Li|$PHL_{1.25}$|Li system even could not make it 30 h. This significant difference again verifies the superior property of $PHL_{1.25}BN_5$. The morphology of Li metal after 40 cycles is presented in Fig. 5c and d. Apparently, there are lots of cracks and dendrites on the Li surface in $PHL_{1.25}$ system (Fig. 5c), while relatively smooth Li surface without any detectable dendrites structure can be observed in $PHL_{1.25}BN_5$ system. To explore whether the cycling stability contributed by interfacial engineering, the compositions of the interface layers from the cycled Li metal surface was studied by X-ray photoelectron spectroscopy (XPS). As shown in Figs. 5e and S0, the interface layer is mainly composed of organic and inorganic substances in both electrolyte systems, such as C-F, C—N, C—C, C—O, LiF, Li_3N and Li_2CO_3. These organic/inorganic components may provide promising ionic conductivity, excellent electrical insulation, and outstanding mechanical properties. Especially, the appearance of LiF and Li_3N in solid electrolyte interphase (SEI) can effectively reduce the diffusion barrier of Li^+ ions through SEI, facilitating uniform migration and deposition of Li^+ ions along the Li metal interface [50–56]. It can be found that the intensity of LiF in $PHL_{1.25}BN_5$ system is much higher than that in $PHL_{1.25}$ system. The quantitative analysis on all components is shown in Table S2. The F content in $PHL_{1.25}$ system is 7.92 %; it increases to 14.96 % (almost two times) in $PHL_{1.25}BN_5$ system, indicating a fluorine-rich interfacial phase formed in later system, which is not only a robust interface, but also a fast Li^+ transportation interface [57]. The contents of N and S also increase in $PHL_{1.25}BN_5$ system, but the contents of C and O decreases; implying that more inorganic components dominate in $PHL_{1.25}BN_5$ system comparing to $PHL_{1.25}$ system. In addition, h-BN can also participate in the formation of the SEI. As presented in Fig. S21, B-containing inorganic salt (Li_xBO_y) appears at around 190.5 eV, which is an effective inorganic component to prevent lithium dendrites [58–60]. To further reveal the distribution of these components in SEI, time-of-flight second

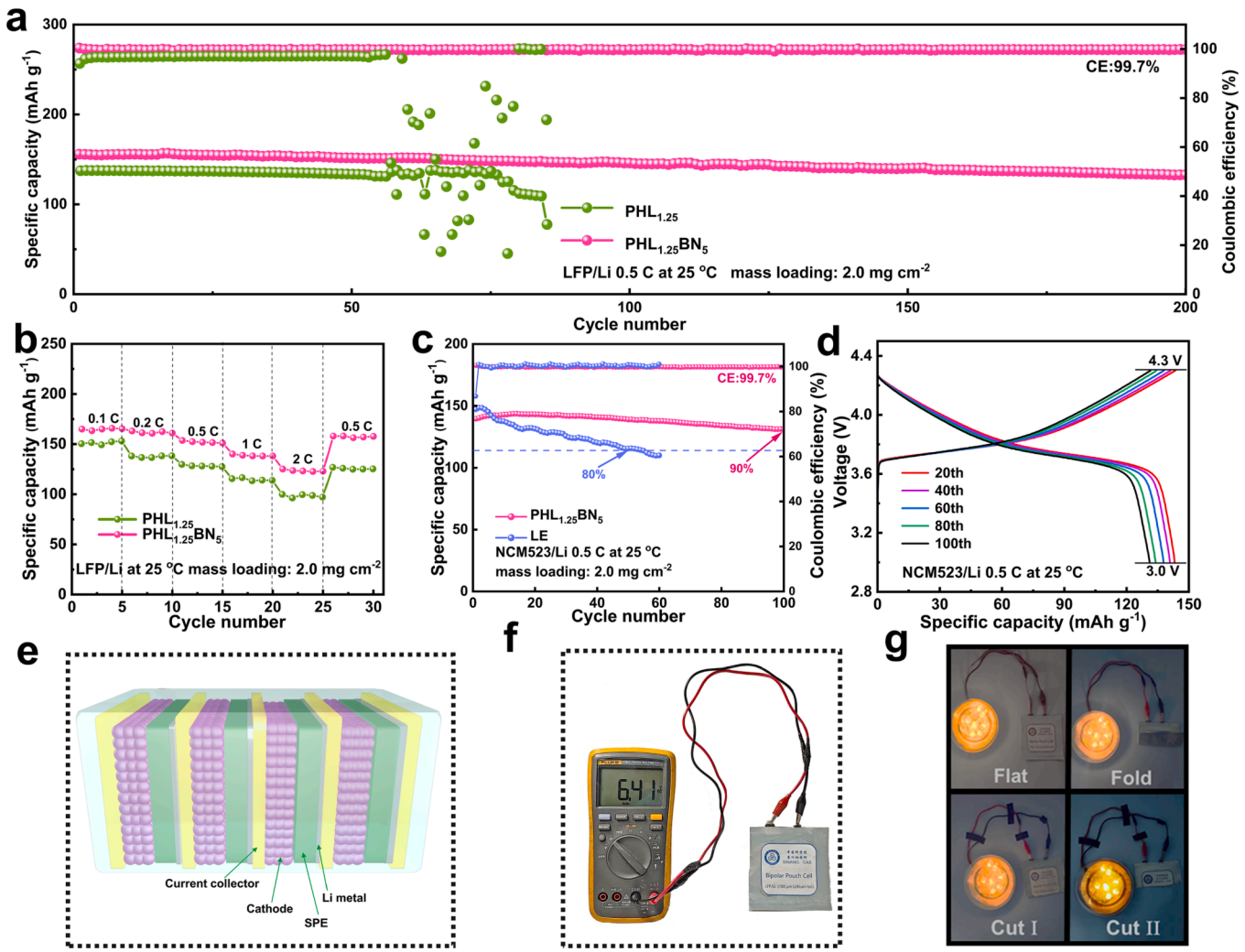

Fig. 6. (a) Cycling performances of LFP/Li cells with $PHL_{1.25}$ and $PHL_{1.25}BN_5$ electrolytes at 25 °C. (b) Rate capability of LFP/Li batteries with two different electrolytes. (c) Cycling performance of NCM/Li cell at 0.5C with $PHL_{1.25}BN_5$ and liquid electrolyte. (d) Discharge/charge profiles of NCM/Li cell with $PHL_{1.25}BN_5$ electrolyte. (e) The schematic diagram of the bipolar pouch cell. (f) Picture of the LFP|$PHL_{1.25}BN_5$|Li bipolar pouch cell with a high output voltage of 6.41 V. (g) Images of the bipolar pouch cell illuminating LED under different abuse tests.

ions mass spectrometry (TOF-SIMS) was performed for both electrolyte systems. As shown in Fig. S22, the signal of LiF_2 is higher in $PHL_{1.25}BN_5$-derived SEI than that in the $PHL_{1.25}$-derived SEI at different sputter times, indicating a LiF-rich SEI layer formed in $PHL_{1.25}BN_5$ system. Correspondingly, the 3D reconstruction of LiF_2 distribution map clearly displays that LiF is much dense in $PHL_{1.25}BN_5$-derived SEI than that in the $PHL_{1.25}$-derived SEI, well matching with XPS results. Other components show similar distribution in these two systems (Figs. S23 and S24). As a consequence, it can be inferred that a large amount of LiF is formed from the decomposition of AGGs in $PHL_{1.25}BN_5$ system.

To demonstrate its great potential in solid-state LMBs, $PHL_{1.25}BN_5$ was applied in $LiFePO_4$/Li (LFP/Li) and $LiNi_{0.5}Co_{0.2}Mn_{0.3}O_2$/Li (NCM523/Li) systems. As shown in Fig. 6a, LFP/Li cell with $PHL_{1.25}BN_5$ delivers an initial discharge capacity of 156 mAh/g at 25 °C and a high Coulombic efficiency (CE) of 99.7 %. Even after cycling 200 cycles, the discharge capacity can still remain 85 % of initial discharge capacity (133 mAh/g), demonstrating the excellent cycle stability. In contrast, the LFP/Li cell with $PHL_{1.25}$ can only achieve a discharge capacity of 136 mAh/g with a poor CE of 96 %, and finally it only works for 60 cycles. The superior performance of $PHL_{1.25}BN_5$ is probably contributed by the fast Li^+ transferring kinetics between $PHL_{1.25}BN_5$ and electrodes, as evidenced by its smaller interface resistance (110 Ω) comparing to $PHL_{1.25}$ system (235 Ω) (Fig. S25). From voltage/capacity profiles, it can also clearly observe that the overpotential of LFP|$PHL_{1.25}BN_5$|Li is much lower that of LFP|$PHL_{1.25}$|Li (Fig. S26). Moreover, the overpotential of LFP|$PHL_{1.25}$|Li increases while cycling, i.e., 0.05 V at 1st cycle, 0.13 V at 80th cycle, while the overpotential of LFP|$PHL_{1.25}BN_5$|Li keeps still along cycling up to 200 cycles. The rate performances again demonstrate the superior property of $PHL_{1.25}BN_5$. As shown in Fig. 6b, LFP|$PHL_{1.25}BN_5$|Li delivers a discharge capacity of 165, 163, 154, 140 and 125 mAh/g at 0.1, 0.2, 0.5, 1 and 2C, respectively; it can return to 156 mAh/g when the current density is back to 0.5C, which is much higher than those obtained in $PHL_{1.25}$ system. Correspondingly, the voltage/capacity profiles in Fig. S27 again verifies that $PHL_{1.25}BN_5$ presents lower overpotentials than those of $PHL_{1.25}$ system at different rates, well explaining the poor rate performance of $PHL_{1.25}$ system.

Considering the good electrochemical stability of $PHL_{1.25}BN_5$ (~4.8 V), high-voltage NCM cathode (4.3 V) was used here to pair with $PHL_{1.25}BN_5$ for further exploring its potential applications. As shown in Fig. S28, the interface resistance of $PHL_{1.25}BN_5$ and $PHL_{1.25}$ are 101 and 203 Ω, respectively in NCM system, indicating that the former system may deliver a better electrochemical performance than $PHL_{1.25}$ system. To further evaluate the superiority of $PHL_{1.25}BN_5$, commercial liquid electrolyte (LE, 1 M $LiPF_6$ dissolving in ethylene carbonate (EC) and diethylene carbonate (DEC) with 1/1 vol ratio) was used here as a control sample. In Fig. 6c, it can be found that NCM523|LE|Li system

delivers an initial discharge capacity of 149 mAh g^{-1}, higher than that of NCM523|$PHL_{1.25}BN_5$|Li system (140 mAh g^{-1}); however, it decays quickly to 118 mAh/g at 50^{th} cycles (80 % capacity retention), much lower than that of $PHL_{1.25}BN_5$ system (136 mAh/g, 96 % capacity retention). Impressively, For $PHL_{1.25}BN_5$ system, the capacity retention of NCM523|$PHL_{1.25}BN_5$|Li can reach as high as 90 % (127 mAh/g) after 100 cycles, well demonstrating the excellent cycle stability of $PHL_{1.25}BN_5$ over LE. The corresponding voltage/capacity profiles shown in Fig. 6d again display the outstanding antioxidation capability of $PHL_{1.25}BN_5$ compared to LE at high voltage system along cycling.

Considering the excellent high-temperature resistance of BN, NCM|$PHL_{1.25}BN_5$|Li battery was performed at high temperature to investigate its high temperature performance. As shown in Fig. S29, the discharge capacity keeps stable at around 150 mAh g^{-1} after 50 cycles at 0.5C under 60 °C, well demonstrating that $PHL_{1.25}BN_5$ can work functionally under high temperature. Meanwhile, benefiting from this solid-state $PHL_{1.25}BN_5$ electrolyte, the bipolar pouch cell can be easily realized. The schematic illustration of bipolar structure is present in Fig. 6e. Comparing with the parallel connection of cells, which is normally used in current commercial pouch cells, bipolar cells can output high voltage, which is a big advantage for practical application. As presented in Fig. 6f, the bipolar pouch cell with two units have been achieved and its voltage output reaches to 6.41 V, which is exactly-two times high of one LFP/Li unit. Except the high-voltage output, sold-state battery also behaves well in terms of flexibility and safety. It can be found that our bipolar pouch cell can light up a tulip light-emitting diodes (LEDs) even after folding and cutting, as evidenced by the pictures shown in Fig. 6g, well revealing the super safety of this $PHL_{1.25}BN_5$-based solid-state batteries. This flexible and safe $PHL_{1.25}BN_5$-based battery with high-voltage output may be suitable for the future applications in wearable electronics.

3. Conclusion

In summary, a high-performance solid-state electrolyte has been achieved by BN-assisted high concentrated PVDF-HFP/LiTFSI. The interaction between BN and the C-F bond in PVDF-HFP not only accelerates the transport of Li^+ along the chain segment, but also creates the internal cluster channel by AGG solvation structure. With these two types of Li^+ transport channels, $PHL_{1.25}BN_5$ exhibits high ionic conductivity (0.37 mS cm^{-1} at 25 °C) and high Li^+ transference number (0.63) and wide electrochemical window (4.8 V). As a result, Li|$PHL_{1.25}BN_5$|Li can be cycled for 1100 h at 0.05 mA cm^{-1}, 800 h at 0.1 mA cm^{-1} and 600 h at 0.2 mA cm^{-1}. Experiments verifies that the superior performance of $PHL_{1.25}BN_5$ is contributed by the high Li^+ transportation kinetics in solid-state electrolyte phase and LiF-rich SEI as well as the robust mechanical property of SEI, which effectively suppresses the dendrites formation. Applying $PHL_{1.25}BN_5$ in LFP/Li and high-voltage NCM/Li systems, both solid-state battery systems could achieve impressive CE of 99.7 % at 0.5C under 25 °C. Even after 100 cycles in high voltage NCM/Li system, the capacity retention can be still up to 90 %. Moreover, the $PHL_{1.25}BN_5$-based pouch cell can be easily assembled into bipolar structure, achieving not only high-voltage output of 6.41 V, but also excellent safety under cutting. These results well demonstrate the great potential of $PHL_{1.25}BN_5$ in future applications.

Declaration of Competing Interest

The authors declare that they have no known competing financial interests or personal relationships that could have appeared to influence the work reported in this paper.

Data availability

Data will be made available on request.

Acknowledgements

The financial support from the National Natural Science Foundation of China (22075313), Guangdong Basic and Applied Basic Research Foundation (2022A1515140165), Outstanding Youth Fund of Jiangxi Province (20192BCB23028) and Jiangxi Double Thousand Talent Program (JXSQ2019101072) is acknowledged.

References

[1] X. Zheng, J. Wei, W. Lin, K. Ji, C. Wang, M. Chen, Bridging Li7La3Zr2O12 nanofibers with poly (ethylene oxide) by coordination bonds to enhance the cycling stability of all-solid-state Lithium Metal Batteries, ACS Appl. Mater. Interfaces 14 (4) (2022) 5346–5354, https://doi.org/10.1021/acsami.1c21131.

[2] W. Zha, W. Li, Y. Ruan, J. Wang, Z. Wen, In situ fabricated ceramic/polymer hybrid electrolyte with vertically aligned structure for solid-state lithium batteries, Energy Storage Mater. 36 (2021) 171–178, https://doi.org/10.1016/j.ensm.2020.12.028.

[3] K. He, S.H.S. Cheng, J. Hu, Y. Zhang, H. Yang, Y. Liu, W. Liao, D. Chen, C. Liao, X. Cheng, Z. Lu, J. He, J. Tang, R.K.Y. Li, C. Liu, In-situ intermolecular interaction in composite polymer electrolyte for ultralong life quasi-solid-state lithium metal batteries, Angew. Chem. Int. Ed. 60 (21) (2021) 12116–12123, https://doi.org/10.1002/anie.202103403.

[4] A. Hu, F. Li, W. Chen, T. Lei, Y. Li, Y. Fan, M. He, F. Wang, M. Zhou, Y. Hu, Y. Yan, B. Chen, J. Zhu, J. Long, X. Wang, J. Xiong, Ion transport kinetics in low-temperature lithium metal batteries, Adv. Energy Mater. 12 (42) (2022), 2202432, https://doi.org/10.1002/aenm.202202432.

[5] D. Zhang, Z. Liu, Y. Wu, S. Ji, Z. Yuan, J. Liu, M. Zhu, In situ construction a stable protective layer in polymer electrolyte for ultralong lifespan solid-State lithium metal batteries, Adv. Sci. 9 (12) (2022), 2104277, https://doi.org/10.1002/advs.202104277.

[6] X. Zhang, S. Wang, C. Xue, C. Xin, Y. Lin, Y. Shen, L. Li, C.W. Nan, Self-suppression of lithium dendrite in all-solid-state lithium metal batteries with poly (vinylidene difluoride)-based solid electrolytes, Adv. Mater. 31 (11) (2019), 1806082, https://doi.org/10.1002/adma.201806082.

[7] L.M. McGrath, J. Jones, E. Carey, J.F. Rohan, Ionic liquid based polymer gel electrolytes for use with germanium thin film anodes in lithium ion batteries, ChemistryOpen 8 (12) (2019) 1429–1436, https://doi.org/10.1002/open.201900313.

[8] R. Chen, Q. Li, X. Yu, L. Chen, H. Li, Approaching practically accessible solid-state batteries: stability issues related to solid electrolytes and interfaces, Chem. Rev. 120 (14) (2020) 6820–6877, https://doi.org/10.1021/acs.chemrev.9b00268.

[9] C. Zhao, Y. Pan, R. Li, A. Hu, B. Zhou, M. He, J. Chen, Z. Yan, Y. Fan, N. Chen, M. Liu, J. Long, A safe anode-free lithium metal pouch cell enabled by integrating stable quasi-solid electrolytes with oxygen-free cathodes, Chem. Eng. J. 463 (2023), 142386, https://doi.org/10.1016/j.cej.2023.142386.

[10] H. Tu, L. Li, Y. Hu, Y. Zhang, Y. Wang, W. Huang, Z. Ren, H. Lin, M. Liu, Non-flammable liquid polymer-in-salt electrolyte enabling secure and dendrite-free lithium metal battery, Chem. Eng. J. 434 (2022), 134647, https://doi.org/10.1016/j.cej.2022.134647.

[11] K. Pan, L. Zhang, W. Qian, X. Wu, K. Dong, H. Zhang, S. Zhang, A flexible ceramic/polymer hybrid solid electrolyte for solid-state lithium metal batteries, Adv. Mater. 32 (17) (2020), 2000399, https://doi.org/10.1002/adma.202000399.

[12] X. Fan, L. Chen, O. Borodin, X. Ji, J. Chen, S. Hou, T. Deng, J. Zheng, C. Yang, S. Liou, K. Amine, K. Xu, C. Wang, Non-flammable electrolyte enables Li-metal batteries with aggressive cathode chemistries, Nat. Nanotechnol. 13 (8) (2018) 715–722, https://doi.org/10.1038/s41565-018-0183-2.

[13] Y. Cui, J. Wan, Y. Ye, K. Liu, L.Y. Chou, Y. Cui, A fireproof, lightweight, polymer-polymer solid-state electrolyte for safe lithium batteries, Nano Lett. 20 (3) (2020) 1686–1692, https://doi.org/10.1021/acs.nanolett.9b04815.

[14] Z. Wang, H. Zhang, J. Xu, A. Pan, F. Zhang, L. Wang, R. Han, J. Hu, M. Liu, X. Wu, Advanced ultralow-concentration electrolyte for wide-temperature and high-voltage Li-metal batteries, Adv. Funct. Mater. 32 (23) (2022), 2112598, https://doi.org/10.1002/adfm.202112598.

[15] T. Zhang, J. Li, X. Li, R. Wang, C. Wang, Z. Zhang, L. Yin, A silica-reinforced composite electrolyte with greatly enhanced interfacial lithium-ion transfer kinetics for high-performance lithium metal batteries, Adv. Mater. 34 (41) (2022), 2205575, https://doi.org/10.1002/adma.202205575.

[16] Z. Zhang, R.G. Antonio, K.L. Choy, Boron nitride enhanced polymer/salt hybrid electrolytes for all-solid-state lithium ion batteries, J. Power Sources 435 (2019), 226736, https://doi.org/10.1016/j.jpowsour.2019.226736.

[17] H. Huo, Y. Chen, J. Luo, X. Yang, X. Guo, X. Sun, Rational design of hierarchical "ceramic-in-polymer" and "polymer-in-ceramic" electrolytes for dendrite-free solid-state batteries, Adv. Energy Mater. 9 (17) (2019), 1804004, https://doi.org/10.1002/aenm.201804004.

[18] J. Zhang, Y. Zeng, Q. Li, Z. Tang, D. Sun, D. Huang, L. Zhao, Y. Tang, H. Wang, Polymer-in-salt electrolyte enables ultrahigh ionic conductivity for advanced solid-

state lithium metal batteries, Energy Storage Mater. 54 (2023) 440–449, https://doi.org/10.1016/j.ensm.2022.10.055.
[19] S. Liu, W. Liu, D. Ba, Y. Zhao, Y. Ye, Y. Li, J. Liu, Filler-integrated composite polymer electrolyte for solid-state lithium batteries, Adv. Mater. 35 (2) (2023), 2110423, https://doi.org/10.1002/adma.202110423.
[20] Y. Shan, L. Li, X. Chen, S. Fan, H. Yang, Y. Jiang, Gentle haulers of lithium-ion-nanomolybdenum carbide fillers in solid polymer electrolyte, ACS Energy Lett. 7 (7) (2022) 2289–2296, https://doi.org/10.1021/acsenergylett.2c00849.
[21] Y. Su, F. Xu, X. Zhang, Y. Qiu, H. Wang, Rational design of high-performance PEO/ceramic composite solid electrolytes for lithium metal batteries, Nano-Micro Lett. 15 (1) (2023) 82, https://doi.org/10.1007/s40820-023-01055-z.
[22] S. Siccardi, J. Amici, S. Colombi, J.T. Carvalho, D. Versaci, E. Quartarone, L. Pereira, F. Bella, C. Francia, S. Bodoardo, UV-cured self-healing gel polymer electrolyte toward safer room temperature lithium metal batteries, Electrochim. Acta. 433 (2022), 141265, https://doi.org/10.1016/j.electacta.2022.141265.
[23] F. Elizalde, J. Amici, S. Trano, G. Vozzolo, R. Aguirresarobe, D. Versaci, S. Bodoardo, D. Mecerreyes, H. Sardon, F. Bella, Self-healable dynamic poly(urea-urethane) gel electrolyte for lithium batteries, J. Mater. Chem. A 10 (23) (2022) 12588–12596, https://doi.org/10.1039/d2ta02239g.
[24] L. Yi, X. Chen, C. Zou, J. Liu, X. Cao, X. Tao, Z. Zang, L. Zheng, L. Liu, X. Wang, Construction and performance of PVDF-HFP-matrix comb-like gel copolymer electrolyte for high-performance quasi-solid-state lithium-metal batteries, J. Energy Storage 68 (2023), 107810, https://doi.org/10.1016/j.est.2023.107810.
[25] M. Gandolfo, J. Amici, L. Fagiolari, C. Francia, S. Bodoardo, F. Bella, Designing photocured macromolecular matrices for stable potassium batteries, Sustain. Mater. Technol. 34 (2022), e00504, https://doi.org/10.1016/j.susmat.2022.e00504.
[26] E. Manarin, F. Corsini, S. Trano, L. Fagiolari, J. Amici, C. Francia, S. Bodoardo, S. Turri, F. Bella, G. Griffini, Cardanol-derived epoxy resins as biobased gel polymer electrolytes for potassium-ion conduction, ACS Appl. Polym. Mater. 4 (5) (2022) 3855–3865, https://doi.org/10.1021/acsapm.2c00335.
[27] Q. Liu, G. Yang, X. Li, S. Zhang, R. Chen, X. Wang, Y. Gao, Z. Wang, L. Chen, Polymer electrolytes based on interactions between [solvent-Li^+] complex and solvent-modified polymer, Energy Storage Mater. 51 (2022) 443–452, https://doi.org/10.1016/j.ensm.2022.06.040.
[28] S. Xu, Z. Sun, C. Sun, F. Li, K. Chen, Z. Zhang, G. Hou, H.M. Cheng, F. Li, Homogeneous and fast ion conduction of PEO-based solid-state electrolyte at low temperature, Adv. Funct. Mater. 30 (51) (2020), 2007172, https://doi.org/10.1002/adfm.202007172.
[29] Z. Xue, D. He, X. Xie, Poly (ethylene oxide)-based electrolytes for lithium-ion batteries, J. Mater. Chem. A 3 (38) (2015) 19218–19253, https://doi.org/10.1039/c5ta03471j.
[30] S. Xu, R. Xu, T. Yu, K. Chen, C. Sun, G. Hu, S. Bai, H.M. Cheng, Z. Sun, F. Li, Decoupling of ion pairing and ion conduction in ultrahigh-concentration electrolytes enables wide-temperature solid-state batteries, Energy Environ. Sci. 15 (8) (2022) 3379–3387, https://doi.org/10.1039/d2ee01053d.
[31] Z. Li, J. Fu, X. Zhou, S. Gui, L. Wei, H. Yang, H. Li, X. Guo, Ionic conduction in polymer-based solid electrolytes, Adv. Sci. 10 (10) (2023), 2201718, https://doi.org/10.1002/advs.202201718.
[32] Y. Yamada, K. Furukawa, K. Sodeyama, K. Kikuchi, M. Yaegashi, Y. Tateyama, A. Yamada, Unusual stability of acetonitrile-based superconcentrated electrolytes for fast-charging lithium-ion batteries, J. Am. Chem. Soc. 136 (13) (2014) 5039–5046, https://doi.org/10.1021/ja412807w.
[33] S. Chen, J. Zheng, L. Yu, X. Ren, M.H. Engelhard, C. Niu, H. Lee, W. Xu, J. Xiao, J. Liu, J.G. Zhang, High-efficiency lithium metal batteries with fire-retardant electrolytes, Joule 2 (8) (2018) 1548–1558, https://doi.org/10.1016/j.joule.2018.05.002.
[34] H. Tu, L. Li, Z. Wang, J. Wang, H. Lin, M. Wang, C. Yan, M. Liu, Tailoring electrolyte solvation for LiF-rich solid electrolyte interphase toward a stable Li anode, ACS Nano 16 (10) (2022) 16898–16908, https://doi.org/10.1021/acsnano.2c06924.
[35] W. Liu, C. Yi, L. Li, S. Liu, Q. Gui, D. Ba, Y. Li, D. Peng, J. Liu, Designing polymer-in-salt electrolyte and fully infiltrated 3D electrode for integrated solid-state lithium batteries, Angew. Chem. Int. Ed. 133 (23) (2021) 13041–13050, https://doi.org/10.1002/anie.202101537.
[36] Y. Hu, L. Li, H. Tu, X. Yi, J. Wang, J. Xu, W. Gong, H. Lin, X. Wu, M. Liu, Janus electrolyte with modified Li+ solvation for high-performance solid-state lithium batteries, Adv. Funct. Mater. 32 (32) (2022), 2203336, https://doi.org/10.1002/adfm.202203336.
[37] Y. Li, L. Zhang, Z. Sun, G. Gao, S. Lu, M. Zhu, Y. Zhang, Z. Jia, C. Xiao, H. Bu, K. Xi, S. Ding, Hexagonal boron nitride induces anion trapping in a polyethylene oxide based solid polymer electrolyte for lithium dendrite inhibition, J. Mater. Chem. A 8 (19) (2020) 9579–9589, https://doi.org/10.1039/d0ta03677c.
[38] C. Zhao, Z. Yan, B. Zhou, Y. Pan, A. Hu, M. He, J. Liu, J. Long, Identifying the role of lewis-base sites for the chemistry in lithium-oxygen batteries, Angew. Chem. Int. Ed. 62 (2023), e202302746, https://doi.org/10.1002/anie.202302746.
[39] P. Zhai, Z. Yang, Y. Wei, X. Guo, Y. Gong, Two-dimensional fluorinated graphene reinforced solid polymer electrolytes for high-performance solid-state lithium batteries, Adv. Energy Mater. 12 (42) (2022), 2200967, https://doi.org/10.1002/aenm.202200967.
[40] L. Li, M. Wang, J. Wang, F. Ye, S. Wang, Y. Xu, J. Liu, G. Xu, Y. Zhang, Y. Zhang, C. Yan, N.V. Medhekar, M. Liu, Y. Zhang, Asymmetric gel polymer electrolyte with high lithium ion conductivity for dendrite-free lithium metal batteries, J. Mater. Chem. A 8 (16) (2020) 8033–8040, https://doi.org/10.1039/d0ta01883j.
[41] J.H. Kim, D.H. Park, J.S. Jang, J.H. Shin, M.C. Kim, S.B. Kim, S.H. Moon, S.N. Lee, K.W. Park, High-performance free-standing hybrid solid electrolyte membrane combined with $Li_{6.28}Al_{0.24}La_3Zr_2O_{12}$ and hexagonal-BN for all-solid-state lithium-based batteries, Chem. Eng. J. 446 (2022), 137035, https://doi.org/10.1016/j.cej.2022.137035.
[42] L. Xu, J. Li, L. Li, Z. Luo, Y. Xiang, W. Deng, G. Zou, H. Hou, X. Ji, Carbon dots evoked Li ion dynamics for solid state battery, Small 17 (39) (2021), 2102978, https://doi.org/10.1002/smll.202102978.
[43] H. Wang, H. Cheng, D. Li, F. Li, Y. Wei, K. Huang, B. Jiang, H. Xu, Y. Huang, Lithiated copper polyphthalocyanine with extended π-conjugation induces LiF-rich solid electrolyte interphase toward long-life solid-state lithium-metal batteries, Adv. Energy Mater. 13 (16) (2023), 2204425, https://doi.org/10.1002/aenm.202204425.
[44] Y. Cao, X. Tang, L. Li, H. Tu, Y. Hu, Y. Yu, S. Cheng, H. Lin, L. Zhang, J. Di, Y. Zhang, M. Liu, Fast Zn2+ mobility enabled by sucrose modified Zn2+ solvation structure for dendrite-free aqueous zinc battery, Nano Res. 16 (3) (2022) 3839–3846, https://doi.org/10.1007/s12274-022-4726-3.
[45] B.L. Li, H. Tu, J. Wang, M. Wang, W. Li, X. Li, F. Ye, Q. Guan, F. Zhu, Y. Zhang, Y. Hu, C. Yan, H. Lin, M. Liu, Electrocatalytic MOF-carbon bridged network accelerates Li+-solvents desolvation for high Li+ diffusion toward rapid sulfur redox kinetics, Adv. Funct. Mater. 33 (13) (2023), 2212499, https://doi.org/10.1002/adfm.202212499.
[46] Z. Wang, L. Shen, S. Deng, P. Cui, X. Yao, 10 μm-thick high-strength solid polymer electrolytes with excellent interface compatibility for flexible all-solid-state lithium-metal batteries, Adv. Mater. 33 (25) (2021), 2100353, https://doi.org/10.1002/adma.202100353.
[47] D.M. Shin, J.E. Bachman, M.K. Taylor, J. Kamcev, J.G. Park, M.E. Ziebel, E. Velasquez, N.N. Jarenwattananon, G.K. Sethi, Y. Cui, J.R. Long, A single-ion conducting borate network polymer as a viable quasi-solid electrolyte for lithium metal batteries, Adv. Mater. 32 (10) (2020), 1905771, https://doi.org/10.1002/adma.201905771.
[48] C. Li, S. Zhou, L. Dai, X. Zhou, B. Zhang, L. Chen, T. Zeng, Y. Liu, Y. Tang, J. Jiang, J. Huang, Porous polyamine/PEO composite solid electrolyte for high performance solid-state lithium metal batteries, J. Mater. Chem. A 9 (43) (2021) 24661–24669, https://doi.org/10.1039/d1ta04599g.
[49] Y. Zhai, W. Hou, M. Tao, Z. Wang, Z. Chen, Z. Zeng, X. Liang, P. Paoprasert, Y. Yang, N. Hu, S. Song, Enabling high-voltage "superconcentrated ionogel-in-ceramic" hybrid electrolyte with ultrahigh ionic conductivity and single Li+-ion transference number, Adv. Mater. 34 (39) (2022), 2205560, https://doi.org/10.1002/adma.202205560.
[50] S. Ye, L. Wang, F. Liu, P. Shi, H. Wang, X. Wu, Y. Yu, g-C_3N_4 derivative artificial organic/inorganic composite solid electrolyte interphase layer for stable lithium metal anode, Adv. Energy Mater. 10 (44) (2020), 2002647, https://doi.org/10.1002/aenm.202002647.
[51] F. He, W. Tang, X. Zhang, L. Deng, J. Luo, High energy density solid state lithium metal batteries enabled by sub-5 μm solid polymer electrolytes, Adv. Mater. 33 (45) (2021), 2105329, https://doi.org/10.1002/adma.202105329.
[52] P. Dong, X. Zhang, K.S. Han, Y. Cha, M.K. Song, Deep eutectic solvent-based polymer electrolyte for solid-state lithium metal batteries, J. Energy Chem. 70 (2022) 363–372, https://doi.org/10.1016/j.jechem.2022.02.026.
[53] Q. Zhou, X. Yang, X. Xiong, Q. Zhang, B. Peng, Y. Chen, Z. Wang, L. Fu, Y. Wu, A solid electrolyte based on electrochemical active $Li_4Ti_5O_{12}$ with PVDF for solid state lithium metal battery, Adv. Energy Mater. 12 (39) (2022), 2201991, https://doi.org/10.1002/aenm.202201991.
[54] Y. Li, A. Hu, X. Gan, M. He, Synergy of in-situ heterogeneous interphases tailored lithium deposition, Nano Res. 16 (6) (2023) 8304–8312, https://doi.org/10.1007/s12274-022-5004-0.
[55] A. Hu, W. Chen, Y. Pan, J. Zhu, Y. Li, H. Yang, R. Li, B. Li, Y. Hu, D. Chen, F. Li, J. Long, C. Yan, T. Lei, N, F-enriched inorganic/organic composite interphases to stabilize lithium metal anodes for long-life anode-free cells, J. Colloid Interface Sci. 648 (2023) 448–456, https://doi.org/10.1016/j.jcis.2023.06.021.
[56] A. Hu, W. Chen, X. Du, Y. Hu, T. Lei, H. Wang, L. Xue, Y. Li, H. Sun, Y. Yan, J. Long, C. Shu, J. Zhu, B. Li, X. Wang, J. Xiong, An artificial hybrid interphase for an ultrahigh-rate and practical lithium metal anode, Energy Environ. Sci. 14 (7) (2021) 4115–4124, https://doi.org/10.1039/d1ee00508a.
[57] M. Liu, X. Guan, H. Liu, X. Ma, Q. Wu, S. Ge, H. Zhang, J. Xu, Composite solid electrolytes containing single-ion lithium polymer grafted garnet for dendrite-free, long-life all-solid-state lithium metal batteries, Chem. Eng. J. 445 (2022), 136436, https://doi.org/10.1016/j.cej.2022.136436.
[58] M. Li, Y. Gao, D. Yu, Z. Hu, Z. Liu, X. Wang, Q. Weng, Y. Chen, Y. Zhang, S. Zhang, Boron nitride as an "all-in-one" gelator to immobilize concentrated sulfone electrolyte towards high performance lithium metal batteries, Energy Storage Mater. 59 (2023), 102753, https://doi.org/10.1016/j.ensm.2023.03.031.
[59] W. Xue, M. Huang, Y. Li, Y.G. Zhu, R. Gao, X. Xiao, W. Zhang, S. Li, G. Xu, Y. Yu, P. Li, J. Lopez, D. Yu, Y. Dong, W. Fan, Z. Shi, R. Xiong, C.J. Sun, I. Hwang, W. K. Lee, Y. Shao-Horn, J.A. Johnson, J. Li, Ultra-high-voltage Ni-rich layered cathodes in practical Li metal batteries enabled by a sulfonamide-based electrolyte, Nat. Energy 6 (5) (2021) 495–505, https://doi.org/10.1038/s41560-021-00792-y.
[60] T. Deng, X. Fan, L. Cao, J. Chen, S. Hou, X. Ji, L. Chen, S. Li, X. Zhou, E. Hu, D. Su, X.Q. Yang, C. Wang, Designing in-situ-formed interphases enables highly reversible cobalt-free $LiNiO_2$ cathode for Li-ion and Li-metal batteries, Joule 3 (10) (2019) 2550–2564, https://doi.org/10.1016/j.joule.2019.08.004.